


## Article

# Ultra-Fast Heating Process of Cu-Pd Bimetallic Nanoparticles Unraveled by Molecular Dynamics Simulation

Zhukun Zhou <sup>1</sup>, Xing Guo <sup>1</sup>, Helin Jia <sup>1</sup>, Guangxian Li <sup>1,2</sup>, Xue Fan <sup>3,\*</sup> and Songlin Ding <sup>2,\*</sup> 

<sup>1</sup> School of Mechanical Engineering, Guangxi University, Nanning 530004, China; zhukunzhou@gxu.edu.cn (Z.Z.); 2011391026@st.gxu.edu.cn (X.G.); 2115391026@st.gxu.edu.cn (H.J.); liguangxian@gxu.edu.cn (G.L.)

<sup>2</sup> School of Engineering, RMIT University, Melbourne, VIC 3083, Australia

<sup>3</sup> Materials Genome Institute, Shanghai University, Shanghai 200444, China

\* Correspondence: fanxue2015@shu.edu.cn (X.F.); songlin.ding@rmit.edu.au (S.D.)

**Abstract:** This paper investigates the ultra-fast heating process of Cu-Pd bimetallic nanoparticles from an atomic-scale perspective, which is essential for laser manufacturing processes, such as laser cladding and selective laser melting. The behavior of high surface ratio nanoparticles during these processes is strongly influenced by their properties and the heating process, which is governed by atomic dynamics. Previous studies have mainly focused on the combination process in pure metallic nanoparticles under slow or isothermal heating, but this work demonstrates that the ultra-fast atomic dynamic process between bimetallic nanoparticles differs significantly. Specifically, in Cu-Pd nanoparticles, the combination process is primarily dependent on the surface atomic motion of the lower melting point particles rather than plastic deformation in the grain boundary between particles. Moreover, the ultra-fast heating process is size-dependent. For small nanoparticles, the atomic kinetics exhibit two different mechanisms depending on temperature: Low-temperature jointing is controlled by localized atomic rearrangement, while high-temperature coalition is governed by the atomic flow of surface atomic melting in the low-temperature melting particle. The combination mechanism is the same for large particles as it is for small particles at high temperatures. The findings of this study provide important insights into the behavior of bimetallic nanoparticles during ultra-fast heating and can inform the development of coat and lubricant.

**Keywords:** Pu-Cu nanoparticles; ultra-fast melting; molecular dynamic simulation; size effect; coat; lubricant



**Citation:** Zhou, Z.; Guo, X.; Jia, H.; Li, G.; Fan, X.; Ding, S. Ultra-Fast Heating Process of Cu-Pd Bimetallic Nanoparticles Unraveled by Molecular Dynamics Simulation. *Coatings* **2023**, *13*, 1078. <https://doi.org/10.3390/coatings13061078>

Academic Editors: Juozas Padgurskas, Raimundas Rukuiža and Audrius Žunda

Received: 6 May 2023

Revised: 3 June 2023

Accepted: 5 June 2023

Published: 11 June 2023



**Copyright:** © 2023 by the authors. Licensee MDPI, Basel, Switzerland. This article is an open access article distributed under the terms and conditions of the Creative Commons Attribution (CC BY) license (<https://creativecommons.org/licenses/by/4.0/>).

## 1. Introduction

Nanoparticles (NPs) have been extensively studied in many areas of science, including metallurgical coating, electrical energy production, catalysis, additive manufacturing, sensing, environmental protection, and biomedicine [1–7] due to their unique size-dependent physical and chemical properties at the nanoscale. Metallic nanoparticles are attractive additives in lubricants for the applications of machinery and aviation fields, primarily due to their unique characteristics of lightweight, higher thermal conductivity, load-carrying capacity, and anti-friction characteristics [8]. Among many kinds of NPs, Cu NPs have received significant attention and have been widely used since they cannot only improve the tribological properties of the base oil, but also display good anti-friction and wear reduction characteristics [9–15]. Recently, many researches focus on the use of noble metals, such as gold, silver, and even palladium, and numerous noble metals have been currently employed to reinforce polymer or composite coatings with the aim of improving mechanical, tribological, and thermal stability properties [16–18]. The noble character of these metals makes them very suitable for preventing the corrosion or reaction of the surfaces in contact [19]. This property qualifies its employment as a good candidate for lubrication of electrical contacts where a sharp increase in the contact resistance results in a fault of the

electronic device, such as micro electromechanical system (MEMS) and nano electromechanical system (NEMS) [20]. For the Pd noble NPs, a decrease in the electrical resistance of the contact was obtained making their application suitable for small connectors and microelectronics [21,22]. In addition, the combinations of Cu and Pd NP were studied in the literature for catalytic reactions including oxygen reduction (ORR) [23] and hydrogen generation reactions [24]. The Cu-Pd bimetallic NPs exhibit enhanced electrocatalytic activity as a result of the interactions between the Cu and Pd NPs and the presence of Cu was believed to avoid inhibition of the Pd active sites in catalytic reactions.

Metal NPs involving lubricants have a higher thermal conductivity than pure oil, which reduces the heat generated by friction and contributes to the mechanical system's stability [25]. However, NPs tend to aggregate together into large-scale clusters due to their high surface energy in the tribological process [26,27]. The tribological performance of lubricants is strongly dependent on the stability and dispersibility of NPs in base fluids. Researchers have concentrated on minimizing or eliminating the agglomerating and sintering behavior of nanoparticles during working [28]. The generally accepted equilibrium Cu-Pd phase diagram contains five phases: A disordered face-centered cubic solid solution  $\text{Cu}_{1-x}\text{Pd}_x$  (A1), a one-dimensional long-period superlattice structure  $\text{Cu}_{21}\text{Pd}_7$  (1D-LPS), intermetallic compounds  $\text{Cu}_3\text{Pd}$  (L12), and Cu-Pd (B2), except for a two-dimensional long-period superlattice structure (2D-LPS) [29,30]. For the Cu-Pd bimetallic nanoparticles, the thermodynamic non-equilibrium phases are difficult to be fully described by the equilibrium Cu-Pd phase diagram. In addition, the traditional phase diagrams do not include surface energy effects, which are important and sometimes even dominant for nanoparticles [31]. The molecular dynamic (MD) simulations provide an effective tool to study the lubrication behavior at the micro-nano scale. The high temperature during lubrication demands the atomic thermal stability properties research of sintering of NP.

The sintering mechanism of Cu and Pd NPs has been extensively studied by experimental and molecular simulations. Most of the attention has been given to studying the sintering of pure metal nanoparticles under isothermal heating nowadays [32]. Zhang et al. [33] reported that the as-synthesized Cu nanoparticles, as a water-based lubricant additive, can significantly improve the tribological properties of distilled water, and some Cu nanoparticles in the solution accelerate the heat transfer process, which also results in good tribological properties. Yuan et al. [34] found that the composite lubrication system with the modified copper nanoparticles applied as the lubricant additives exhibits good friction-reduction and wear-resistance on the tribological properties of cylinder liner-piston ring. Moreover, Pd nanoparticles have a host of attractions at the same time. Sánchez-López et al. [35] gained effective anti-wear performance specimen by using surface-modified Pd nanoparticles (2 nm-core size) and the excellent anti-wear response is explained by the formation of a metal-containing transfer film and their action as counter-face spacers avoiding direct contact by the experiment. Moreover, they reported that the Pd nanoparticles are useful as a thin solid lubricant film in reciprocating motion yielding a comparable tribological behavior [36]. In addition, many MD simulations are performed to shed light on Cu and Pd nanoparticles. Kart et al. [37] reported that the melting temperatures of the copper nanoparticles increased as the size of the nanoparticles increases during the MD simulation method utilizing the Quantum Sutton-Chen (Q-SC) many-body force field. Kalteh et al. [38] reported on the convective heat transfer of an argon-copper nanofluid in a copper nanochannel under Poiseuille flow conditions. The result showed that the aggregation of nanoparticles reduces the mobility of the atoms and the amount of solid-like layer around the nanoparticles, which reduces the Nusselt number. Marashi et al. [39] studied the stability and melting behavior of palladium clusters with 2–20 shells of cub and icosahedron structures using MD simulation and embedded-atom method (EAM) force field. The result showed that the cub clusters of intermediate size transform to icosahedron at elevated temperatures and both cub and icosahedron are stable up to the melting point for larger sizes. Valencia et al. [40] reported that nanocrystalline shells at large strains of a constant flow stress regime are observed even for deformations as high as 80% due to the

grain boundary activity during the MD simulation of Pd hollow nanoparticles. However, it is expected that the sintering mechanism will differ from the case of pure metals due to the differing physical and chemical properties and their interactions when different metals are involved in lubrication behavior involving the fast heating rate in high temperature. Wang et al. [41] observed that the Cu nanoparticle is enriched on the Cu-Pd nanoalloy surfaces at the high Cu/Pd ratio during the growth of Cu-Pd nanoalloys encapsulated in carbon-shell, which is attributed to the relatively low surface free energy of Cu. Delhommelle et al. [42] found that the free energy of nucleation strongly depends on the composition of the alloy and the free energy barrier for the equimolar alloy is more than two times larger than the pure metals during the MD simulation of the nucleation process of Cu and Pd nanoalloy. Celik et al. [43] reported the forming of crystal phase related to the presence of crystal-type polyhedrons and Cu concentration in the research of the crystallization mechanism from amorphous matrix during the annealing progress in Cu-Pd and Cu-Pt alloy systems by using MD simulation with the embedded-atom method.

In this study, we investigated the sintering process of Cu-Pd bimetallic NP with diameters ranging from 2 nm to 18 nm at high heating rates using molecular dynamic simulations based on the second nearest-neighbor modified embedded-atom method (2NN MEAM). Our MD simulations provide atomic-level insights into the entire dynamic sintering process. By analyzing various parameters, such as average atomic potential energy, radial distribution functions (RDF), non-Gaussian parameters (NGP), radius of gyration, shrinkage ratio, and mean square displacement (MSD) for systems with different nanoparticle sizes, we examined the atomic motion of atoms under different temperatures at various positions within each particle. Using CNA structure, particle shear strain, and structural snapshots, we analyzed the sintering dynamic properties of the Cu-Pd bimetallic NP in detail. The methodology, results, and discussions will be presented in the following sections. Moreover, the result may provide atomic understanding for some specific applications of Cu-Pd bimetallic NP in lubricant.

## 2. Materials and Methods

To simulate ultra-fast melting and examine atomic-level properties, we conducted classical MD simulations using the large-scale atomic/molecular massively parallel simulator (LAMMPS) [44]. The interactions potential among bimetallic atoms were described by the second nearest-neighbor modified embedded-atom method, as reported by Ga-Un Jeong et al. [45]. We built a bulk face-centered cubic lattice of Cu with the lattice parameter of 3.615 Å and a decent center cubic lattice of Pd with a lattice parameter of 3.89 Å [46], and periodical boundary conditions were imposed in the simulations. The ultra-fast melting process was simulated under the NVT ensemble, utilizing a 1 fs time step. During simulation, the number of atoms  $N$ , volume  $V$ , and temperature  $T$  remained constant, and data were recorded at every 2000 ps intervals. The desired temperature and ambient pressure were maintained by Noe-Hoover thermostat [47] and Berendsen approach [48], respectively. Atomic motion equations were integrated using the Verlet-velocity algorithm [49] with a 1 fs time step.

Prior to the simulation of nanoparticle sintering, the two nanoparticles range from 2 nm to 18 nm in the initial structures with surface separation distance of 0.2 nm apart, and were first fully relaxed using the NVT ensemble at 300 K for 300 ps with a time step of 1 fs. Upon starting MD simulations, all nanoparticles were first quasi-statically relaxed to a local minimum energy state through the conjugate gradients method [50]. After full relaxation, the nanoparticles were subjected to a continuous heating process. During the simulation of sintering process using NVT ensemble, the whole system was heated from 300 K to 2500 K at the heating rate of 1 K/ps and thermodynamic data were output every 1000 frames. We plot the temperature and time at the bottom and top of the figures for convenience. The change in surface facets, the common neighbor analysis (CNA) [51], and the atomic strain analysis were qualitatively and quantitatively analyzed by the OVITO open visualization tool and OVITO Python open-source scripts [52].

We should mention that the angular momentum of nanoparticles was adjusted to zero every 100 steps by subtracting a rotational component from each atom. The anisotropic characteristics of crystalline materials can easily cause shape changes and drift of the center of mass, leading to the spontaneous rotation of the particles, which is commonly observed in the simulation of crystalline NP [53]. The fixed angular momentum does not affect the motions on the surface and simplifies the analysis process.

As the crystal structure of Cu is face-centered cubic (FCC), the lattice constant is 0.3606 nm, and the Cu-Cu bond length is about 0.258 nm. On this basis, we define the Cu atoms with a distance of less than 0.258 nm from the surface of the nanoparticle as surface Cu atoms, whereas the atoms with a distance greater than 0.258 nm from the surface of the Cu nanoparticle are defined as internal Cu atoms [54]. The defining of Pd NP surface and internal atoms follows the same method.

In this study, we simulated the melting point of Cu and Pd NPs with varying sizes by calculating the potential energy changes during an ultra-fast heating process. In addition, the melting point of each case was estimated based on the average potential energy and temperature curve. By comparing the calculated melting point and NP size, we were able to establish a relationship between the NP size and melting point, and thus explore the size effect of NP.

The radial distribution function (RDF) is the probability distribution to find the center of an atom in a given position at a radial distance  $r$  from the center of a reference sphere, which can describe the one-dimensional order of a homogeneous system [55,56]. The RDF is defined as:

$$g(r) = \frac{V}{N} \frac{n(r)}{4\pi r^2 \Delta r} \quad (1)$$

where  $N$  is the total number of atoms,  $V$  is the volume of the system, and  $n(r)$  represents the number of atoms in the thickness of  $\Delta r$  at the radius ( $r$ ) of the nanoparticles.

In the MD simulation of NP, the radius of gyration  $R_g$  is calculated as [57]:

$$R_g = \sqrt{\frac{1}{M} \sum_{i=1}^N m_i (r_i - r_{cm})^2} \quad (2)$$

where  $M$  is the total mass of atoms in the simulation system,  $m_i$  is the mass of the atom  $i$ ,  $r_i$  is the position of the atom  $i$ , and  $r_{cm}$  is the center of mass position.

The shrinkage ratio  $S_r$  is an important indicator of the degree of sintering, the shrinkage ratio  $S_r$  is calculated as [58]:

$$S_r = \frac{\Delta L}{L_0} = \frac{L_0 - L}{L_0} \quad (3)$$

where  $L_0$  and  $L$  are the distance between the center of the initial moment (the temperature is 300 K) and the moment of  $t$ , respectively.  $\Delta L$  is the difference between  $L_0$  and  $L$ .

The mean square displacement (MSD) can be calculated by taking the average of the square displacement over all atoms in the simulation, which is defined as [59]:

$$MSD = \frac{1}{N} \sum_{i=1}^N [r_i(t) - r_i(0)]^2 \quad (4)$$

where  $N$  represents the total number of atoms,  $r_i(0)$  and  $r_i(t)$  represent the positions of the atom at the time constants 0 and  $t$ , respectively. The MSD is monitored in the simulation to describe the displacement of atoms during the ultra-fast sintering process.

To describe correlations between velocities at different times along an equilibrium trajectory, the position auto-correlation function (XACF) is an equilibrium property of a system, which is defined as [60]:

$$XACF_i = \frac{\langle [r_i(t) \times r_i(0)] \rangle}{\langle [r_i(0) \times r_i(0)] \rangle} \quad (5)$$



where  $r_i(t)$  is the position of  $i_{th}$  atom at time  $t$  and  $\langle \rangle$  denotes the ensemble average. The position at the initial condition is represented with  $r_i(0)$ . XACF describes the degree of correlation between time  $t$  and initial time, which can provide information about the motion of atoms in the molecular system, such as the diffusion behavior and viscosity of atoms.

The non-Gaussian parameter (NGP) or  $\alpha_2$  measures the statistical heterogeneity of an underlying random variable, which is defined as [61,62]:

$$\alpha_2 = \frac{3\langle \Delta r^4 \rangle}{5\langle \Delta r^2 \rangle^2} - 1 \quad (6)$$

where  $\langle \rangle$  denotes the ensemble average; therefore,  $\langle \Delta r^4 \rangle$  and  $\langle \Delta r^2 \rangle$  could be calculated based on the position of atom in the generated dump file.

During the continuous heating process of a specific system, if the MSD value is homogeneous or the displacement from each atom remains statistically the same by following the Gaussian distribution, then the value of  $\alpha_2$  is zero. However, if certain atoms start to execute the displacements that are larger than other atoms or show non-Gaussian distribution, such as in surface disordering, the value of  $\alpha_2$  starts to rise [63]. Thereafter, we can capture sensitively the starting temperature of surface disordering and related melting processes according to the change in  $\alpha_2$ .

### 3. Result and Discussion

#### 3.1. Macroscopic Sintering Process

##### 3.1.1. The Potential Energy Evolution and Structure Evolution

Figure 1 illustrates the atomic potential energy of NPs with diameters ranging from 2 nm to 18 nm at a heating rate of 1 K/ps. The sum of atoms in the NPs range from 646 to 466,108. To better demonstrate the variation of average particle potential energy with temperature under different sizes, corresponding curves were shifted along the Y-axis to prevent overlapping. As shown in the figure, the atomic average potential energy curve is divided into two types based on NP size, indicating the size effect of NP. The average particle potential energy before the first peak decreases as the particle radius increases due to the decrease in surface/volume atomic ratio. The melting region shifts to a higher temperature as for the larger NP, consistent with the size-dependent single NP melting process. This is due to the fact that the atomic cohesion energy increases with the increase in coordination number in larger samples, following the increase in surface/volume atomic ratio. However, the average potential energy curve shows a single peak when the diameter is below 4 nm. In the low-temperature stage, the curve increases linearly with temperature until it reaches a certain temperature, then jumps significantly due to NP melting, followed by a potential energy drop and decrease in a certain region due to the large mixing enthalpy of Pd and Cu atoms during the sintering process [64]. Since the non-melting atomic proportion of Pd in small samples is limited, the melting peak of Pd is covered by the Cu and Pd atomic mixing process. Above 6 nm, the average potential energy curve shows two peaks related to the melting of Cu and Pd NPs during the sintering process, in contrast to the pure nanoparticle sintering process. The slopes of the potential energy curve before the Cu surface melting region near the first peak are similar, with a significant nonlinear region, in contrast to the sharp energy jumps in the slow heating and step-like heating process. The nonlinear region corresponds to the solid-to-liquid transition process, featuring the atomic melting and sintering kinetics under an ultra-fast heating rate. The region between two peaks corresponds to the coexistence of the liquid-state Cu NP and the solid state in the core part of Pd NP. Under the influence of the mixing process between two different atoms, the melting dynamic of the Pd NP deviates from the pure Pd NP melting process. In contrast to the average atomic potential energy curve before the first peak, the value between the first and second peak increases with the rise in NP diameter.

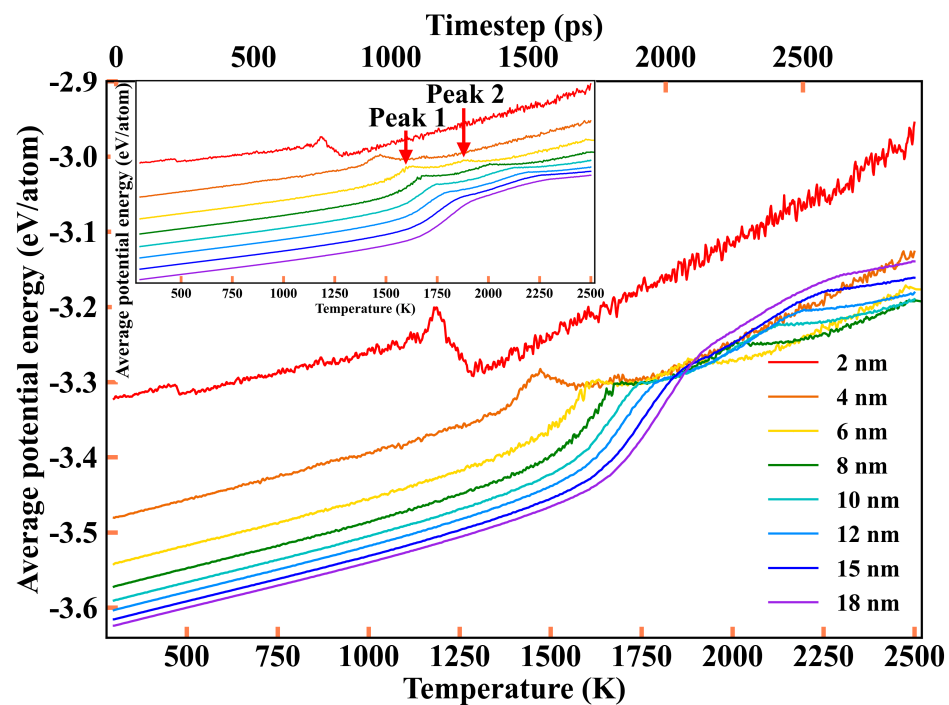


**Figure 1.** The average potential energy of the whole system during the heating process of different sizes. The two red arrows in the inset picture located in the upper left show the melting temperatures of Cu and Pd NP, respectively, and the diameters ranging from 2 nm to 18 nm.

As shown in Figure 2a, the temperatures corresponding to the first and second peaks of the potential energy curve (Figure 1) both show an increasing trend as the size increases. Among the NPs ranging from 2 nm to 4 nm, the first peak and the second peak of the potential energy curve change most significantly. When the diameter of NP exceeds 6 nm, the three curves' growth rate slows down with continued size increase and becomes a linear relationship between the temperature and diameter of NP. The melting temperature difference between two NPs is represented by the temperature difference between the first peak and the second peak of the temperature-potential energy curve, which increases with the rising temperature before stabilizing at about 400 K around 10 nm. This stabilization occurs since the melting temperature of NPs difference is the same as the melting temperature difference for these two bulk metals. To describe the homogeneous mixture of these two particles, we chose the stabilized first peak in Cu-Pu partial RDF, as shown in Figure 3d. The size-dependent stabilized RDF curve shown in Figure 2a indicates that the temperature of uniform mixing of two different types of NPs shows a similar trend to the melting temperature of the NPs, but it is slightly higher for Pd NPs. As the diameter of NP increases, the temperature difference between them increases, suggesting that larger NPs require a higher temperature and a longer sintering time. This information can provide theoretical guidance for achieving an appropriate temperature for homogeneous mixing of NPs during the ultra-fast sintering processes.

Moreover, Figure 2b depicts the relationship between the melting temperature and inverse NP diameter. As the inverse diameter of NPs increases, the melting temperature of Cu NP decreases. However, in the case of 2 nm and 4 nm NP, the relationship between temperature and  $D^{-1}$  deviates from the Gibbs–Thomson equation, which suggests that the melting point is proportional to  $D^{-1}$  for the same range of NPs. This deviation is also observed in other systems, such as Ag and Au NP [65], which can be attributed to the larger surface/volume atomic ratio in smaller particles. This difference results in two modes of melting, namely pre-melting for small NP and melting mode for large NP. Consequently, these different melting modes lead to two distinct sintering mechanisms.

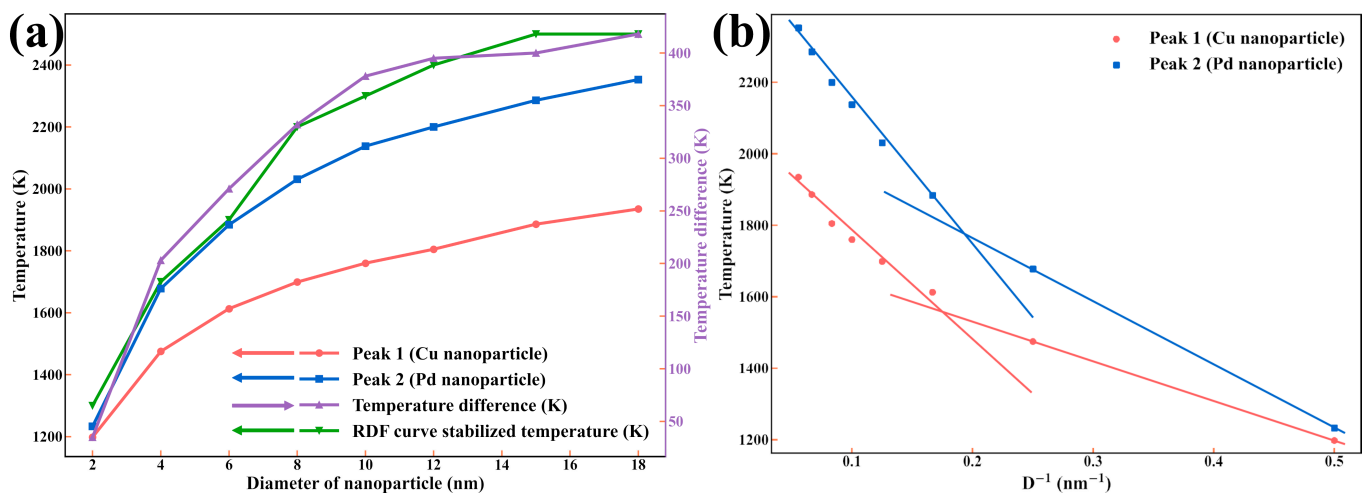


**Figure 2.** (a) The relationship between the first peak's temperature and the size of nanoparticles in Figure 1 (red line), the second peak's temperature and the size of nanoparticles in Figure 1 (blue line), the temperature difference between the first peak and the second peak in Figure 1 (purple line), and the surface RDF curve stabilized temperature of different sizes. (b) The relationship between the inverse of diameter ( $D^{-1}$ ) and the melting temperature.

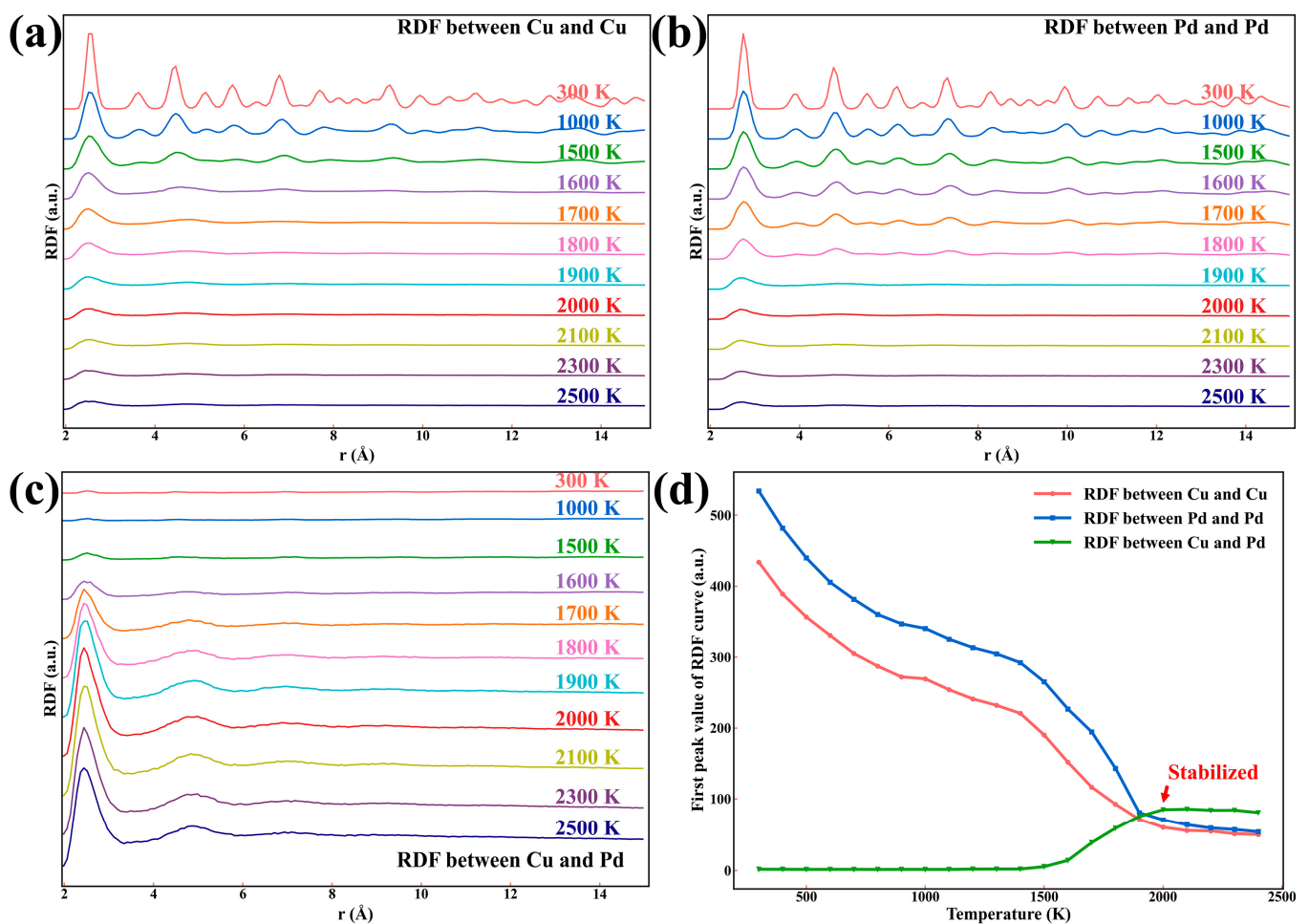


**Figure 3.** The partial RDF of 6 nm Cu-Pd NPs, (a) Cu and Cu, (b) Pd and Pd, (c) Cu and Pd, and (d) the relationship between the first peak and temperature.

### 3.1.2. The Average Crystal Structure Evolution

The melting and sintering process of NPs can also be detected through spatial topological structure information, which provides a more intuitive view of the atomic packing or mixture process. In this paper, the partial RDF is used to facilitate the structure evolution during the ultra-fast heating process. As shown in Figure 3a,b, with an increase in temperature, the peak value remains unchanged, but the curve gradually becomes rougher, and the peak width also increases, indicating an increase in the disorder degree of atoms in the particles as the temperature rises. Moreover, for temperatures below the melting point, the RDF curve of Cu NP has a well-defined peak near 2.58 Å, which represents the distance between the nearest neighboring atoms of the FCC structure of Cu [66]. This offers further confidence and confirms the validity of the adapted potential function for the Cu and Pd mixture system. Additionally, the first peak width of the RDF curve begins to widen, and the second peak disappears when the temperature reaches the melting point, indicating that the volume of disorder structure is primary, and the system has become liquid. Figure 3c shows that the peak of RDF between Cu and Pd becomes notably above 1500 K and the peak height gradually increases as the temperature rises, implying an increase in the number of Cu-Pd pairs. Furthermore, the temperature-dependent first peak for Cu-Cu and Pd-Pd pair decreases gradually with the increasing temperature, while the Cu-Pd pair show the opposite trend. In addition, all RDF values become constant after 2000 K, indicating the homogeneous mixing of the two NPs. Therefore, the starting point of the constant RDF value (RDF stabilized temperature) is a more rigorous variable for evaluating the effective mixing of the NPs rather than the melting temperature. The size dependence of the RDF curve stabilized temperature is presented in Figure 2a.

The RDF curve depicted in Figure 3 illustrates the overall structural changes during the sintering process. Since the surface atoms play a crucial role in determining this process, Figure 4 shows the RDF curve of the surface atoms in Cu NP at the point of the abrupt increase in the sintering neck radius temperature. It is evident that the partial RDF of 2 nm and 4 nm NP differs from the others, indicating that the sintering neck grows under a different mechanism under this temperature. The presence of a large first peak and a second peak in the 2 nm and 4 nm NP suggests that their surface atoms still retain an ordered crystal structure rather than a disordered liquid state with a single broad peak seen in the larger NP. This corresponds to the facet shape of the small NP at 1100 K in Figure 5, as well as the aggregation of Cu atoms at the sintering neck in Figure 6.

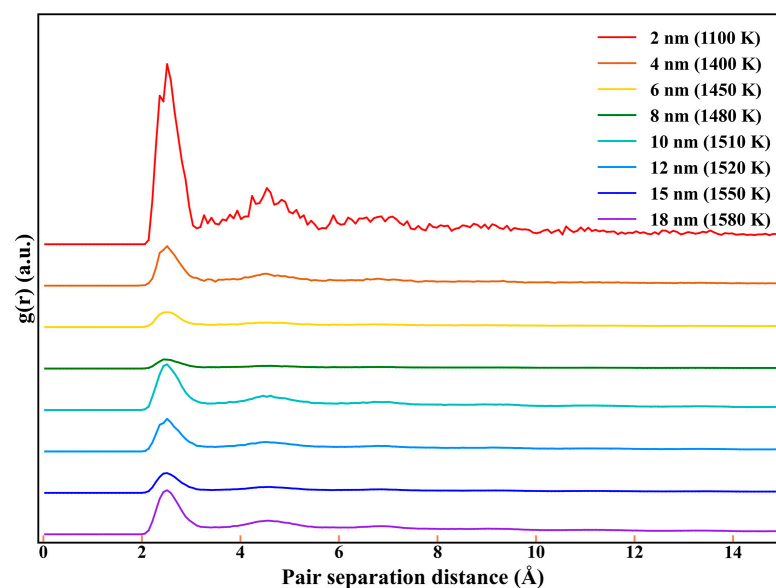


**Figure 4.** The radial distribution function (RDF) curve under the melting temperature of Cu shell part nanoparticle with different diameters.

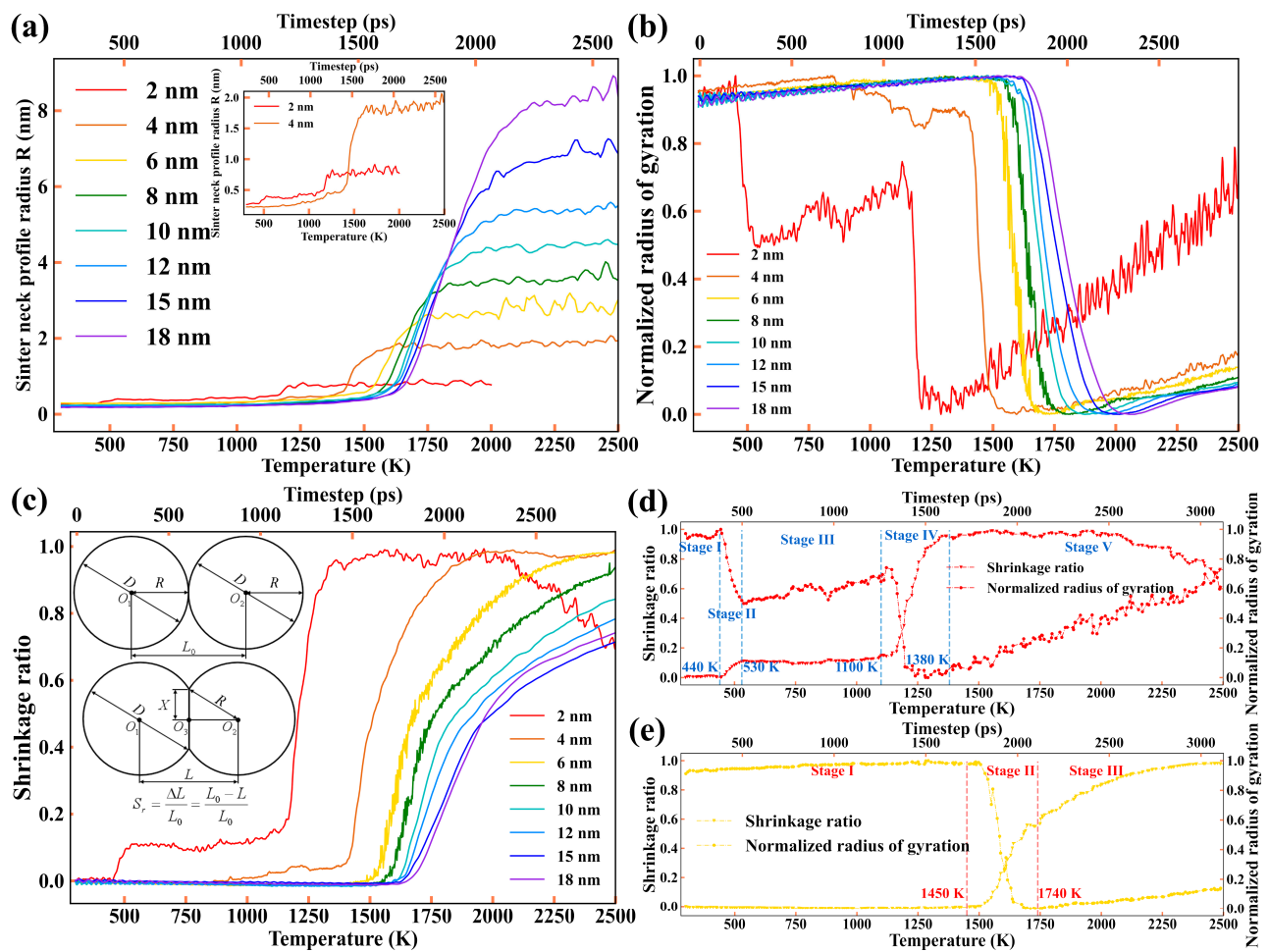


**Figure 5.** (a) The sinter neck profile radius  $R$ , and the insert figure in (a) shows the sinter neck profile radius  $R$  curve of  $D = 2$  nm and  $D = 4$  nm Cu–Pd NPs, (b) the normalized radius of gyration, (c) the shrinkage ratio as a function of temperature during the sintering process of Cu and Pd NP with different diameters ranging from 2.0 to 18.0 nm, (d) the five sintering stages of  $D = 2$  nm Cu and Pd NPs, and (e) the three sintering stages of  $D = 6$  nm Cu and Pd NPs.

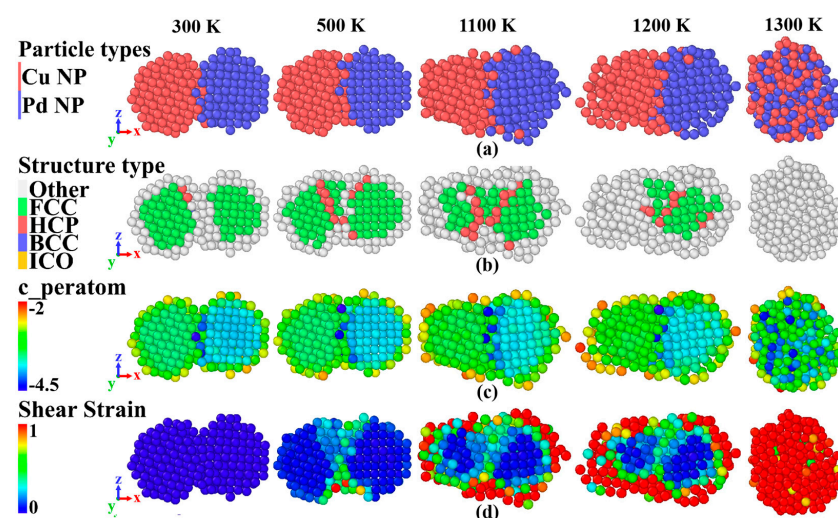


**Figure 6.** (a) The atomic type, (b) the CNA snapshots, (c) the atomic potential energy, and (d) the shear strain of sliced 2 nm Cu–Pd NPs under the temperatures of 300 K, 500 K, 1100 K, 1200 K, and 1300 K.



### 3.1.3. Sintering Neck Radius and Shrinkage Ratio

Figure 5 displays a temperature-dependent analysis of the sintering neck radius ( $X$ ), normalized radius of gyration, and shrinkage ratio. The results show that the sintering process is dependent on the diameter of NP. The insert picture in Figure 5a illustrates the curve of the sintering neck radius ( $X$ ) for 2 nm and 4 nm NP, while the insert picture in Figure 4e describes the calculation method of the shrinkage ratio. For the 2 nm and 4 nm NP, the sintering process shows two steps that can be divided into five stages: Slow fluctuation and slow increase (Stage I), first rapid increase (Stage II), initial stable (Stage III), second rapid increase (Stage IV), and final stable state (Stage V), respectively. In Stage I of 2 nm NP, as shown in Figure 5e, all curves fluctuated within a small range, corresponding to the NP relaxation process. In Stage II, the first rapid growth of the sintering neck commences, which relates to surface reconstruction that forms a lower energy state of the facet shape rather than the sphere shape, which is evident from an atom snapshot. Moreover, the surface reconstruction is a result of localized surface atomic rearrangement elaborated later in this work. Interestingly, many reports have already proven the facet state in small NPs or clusters [67–71]. In Stage III, the surface reconstruction finishes, and the sintering process reaches a stable state with atomic thermal fluctuations. In Stage IV, the neck radius and the normalized radius of gyration undergo the second abrupt increase, while the normalized gyration radius meets an abrupt drop. This phenomenon may relate to the surface atomic pre-melting of Cu NP, and the sintering neck radius ( $X$ ) and shrinkage ratio almost remain constant in Stage V.

With an increase in NP diameter, the sintering process in 6 nm to 18 nm NP can be divided into three stages (as shown in Figure 5e): Slow increase and fluctuation state (Stage I), rapid increase state (Stage II), and stable state (Stage III), respectively. Stage I is similar to the Stage I of 2 nm and 4 nm NPs, but with smaller fluctuations. As the temperature rises, the surface atoms of Cu NPs reach the melting temperature; atom flows near the sintering neck into the neck alley for capillary effect, leading to the abrupt increase in the sintering neck and shrinking rate in Stage II. As seen in Figure 5a, the temperature for the abrupt increase in the sintering neck radius is mostly the same in 6 nm to 18 nm nanoparticles, around 1600 K. In the later part, there exists a sudden increase in the sintering neck radius that relates to the melting of surface atoms, which are almost independent of NP size. The surface pre-melting begins at around 0.7 times of the melting point ( $T_m$ ), and this temperature was considered the theoretical sintered temperature [72,73]. Furthermore, Stage III in larger NPs differs from the smaller ones (2 nm and 4 nm). For the smaller NPs, the melting points of two kinds of NPs are near, and the mixing process finishes quickly. However, for the larger NP, the melting temperature in Cu and Pd NP differs (as seen in Figure 2), and the mixing process experiences a relatively long time. All the curves continue to increase until the melting point of Pd NP, then exhibit a slight increase.

## 3.2. Sintering Mechanism

### 3.2.1. Atomic Characterization

The atomic snapshots displayed in Figure 5 indicate that both Cu and Pd atoms have structured quasi-sphere shape under 300 K. As the temperature increases, the sphere shape gradually turns into a facet shape, and then merges into one sphere particle after melting at around 1300 K. In contrast to the stable sphere shape in larger NPs, the facet shape is supposed to be the stable state in smaller NPs or clusters (2 nm). It has been confirmed by both experiments and theoretical calculations [74,75]. At lower temperature, the surface atoms lack sufficient energy to overcome the energy barrier. Therefore, their atomic potential energy fluctuates in the original position. However, the increasing temperature provides additional energy for surface atom migration, resulting in a facet state, which leads to the sintering neck radius increase shown in Figure 5. To determine the structural changes during the sintering process, we used CNA analysis to describe the atomic structure of the NP (as shown in Figure 6b). The results show that the atoms in the surface and sintering neck are in other atomic types, while the inner atoms remain in an FCC state

at 300 K. As the temperature increases, some hexagonal closest-packed (HCP) structures form in the sintering neck region due to the shear and shuffle of Cu and Pd atoms. This results in a relatively looser structure, larger shear strain, and stress at the sintering neck as shown in Figure 6d. At 1200 K, all Cu atoms turn into other types, corresponding to the melting of Cu NPs in Figure 1. Since the melting temperature of bulk Pd is higher than bulk Cu, the interior of Pd NP remains in an FCC state at 1200 K. After reaching the Pd NP melting temperature, all atoms become other types. Figure 6c shows the atomic potential energy of the NPs. It indicates that the surface atoms have higher energy than the inner ones. Additionally, the potential energy of Pd NP is relatively lower than Cu NP. After interacting with the Cu NP, the Pd atomic potential energy turns into a significantly lower state, which may be ascribed to the large negative mixture enthalpy of Cu-Pd bimetallic nanoparticles [76].

Figure 7 displays the detailed atomic types (a), CNA snapshots (b), atomic potential energy (c), and shear strain (d) of sliced 6 nm Cu-Pd NPs under different temperatures. The atomic type snapshots indicate that both Cu and Pd atoms have a structured sphere shape under 300 K. With an increase in temperature, the NPs remain in a sphere shape, but with a rougher surface, which differs from the 2 nm results. The sintering neck radius increases with the temperature. As shown in the evolution of atomic species in Figure 7a, several Cu atoms on the surface diffuse onto the Pd NP surface before melting, and then the melted Cu atoms wrap around the Pd atoms above the melting temperature of Cu NP. By comparing the atomic species in the sintering neck radius at 1500 K and 1600 K, we can state that the rapid growth of sintering necks is controlled by the Cu atomic flow on the surface of NPs. The atomic flow under melting is governed by the curvature radius, where a larger curvature radius leads to faster atomic flow, as evidenced in the sintering neck radius in Figure 5a. Some hexagonal closest-packed (HCP) structures and disorder structures (the position of dislocations) are present in the sintering neck of Cu NP under 300 K, resulting from plastic deformation during relaxation and ration of the NP. However, during the following sintering process at high temperatures, it seems that the plastic deformation at lower temperatures has limited effect on the ultra-fast sintering process, which differs from sintering in the mono-element sintering at constant temperature. In summary, for the smaller NP, the growth of neck radius is governed by localized atomic diffusion at low temperatures, whereas for the larger NP, the growing sintering neck radius is dominated by atomic flow under NP surface melting.

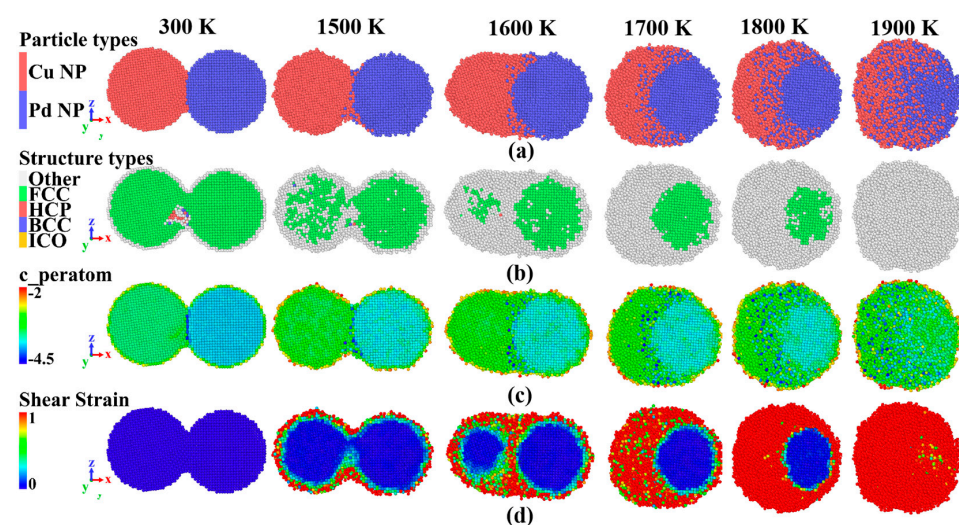


**Figure 7.** (a) The atomic type, (b) the CNA snapshots, (c) the atomic potential energy, and (d) the shear strain of sliced 6 nm Cu–Pd NPs under the temperatures of 300 K, 1500 K, 1600 K, 1700 K, 1800 K, and 1900 K.

### 3.2.2. The Shell Atomic Energy and Motion Pattern

Figure 8a exhibits the temperature dependence of the average atomic potential energy (AAPE). It can be observed that the smaller NPs have higher average atomic potential energy than larger ones. All AAPE curves exhibit a similar pattern, gradually increasing with temperature, then decreasing in a certain temperature range before resuming an increasing trend. The reduction in magnitude correlates with an increase in NP size. For Cu NP with diameters ranging from 6 nm to 18 nm, the transition temperature is approximately constant at 1300–1400 K. This temperature corresponds to 0.65–0.70 of the reported 0.7  $T_m$  criterion considering that the bulk Cu melting point in this study is 1980 K [77]. Therefore, the AAPE transition temperature signifies the melting of shell part atoms. The dotted lines represent the temperature at which the abrupt growth neck radius occurs, which follows the transition temperature. By integrating the results from the atomic snapshots, sintering neck growth occurs due to the flow-melting of atoms. Additionally, since Cu-Pd bimetallic nanoparticles have considerable negative enthalpy, the decrease in AAPE implies an increasing number of Cu atoms shifting toward the Pd NP.

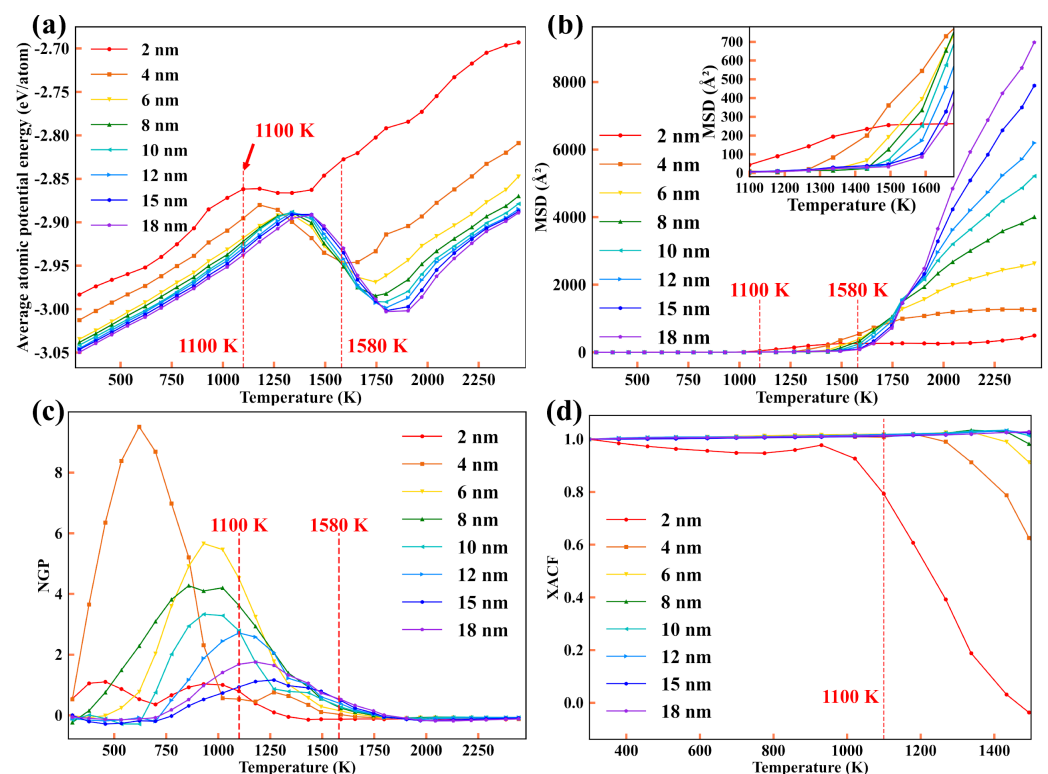


**Figure 8.** The temperature dependence of (a) the average atomic potential energy (AAPE), (b) the mean square displacement (MSD), and the insert figure in (b) shows the MSD curve change temperature under different size, (c) the non-Gaussian parameter (NGP), and (d) the position auto-correlation function (XACF) of 6 nm Cu NPs shell part.

To quantify the atomic motion in detail, we present MSD, NGP, and XACF in Figure 8b–d. The MSD curve depicts the average displacement of shell atoms, indicating limited atomic displacement before melting, with gradual increase afterward. Samples with larger NPs exhibit a greater MSD since they provide more room for atomic movement. NGP is an effective indicator of the number of atoms in various movement patterns. After complete melting, NGP shows a value of zero for all samples, suggesting the random movement of atoms. Except for the 2 nm case, NGP presents a single peak across all ranges, with the peak height reducing with the increasing NP size, while peak temperature increases with the rise in NP diameter. This indicates that larger NPs undergo more random atomic movement, experiencing distinct movement patterns during ultra-fast heating, and corresponding

to the three sintering stages presented in Figure 4e. However, for 2 nm and 4 nm NP, the NGP at low temperature is non-zero, indicating that the atom movement follows certain rules to shape facets as shown in Figure 4d. The double peak for the 2 nm sample signifies two diverse movement patterns during the sintering process, which corresponds to the abrupt growth of sintering necks. The XACF curve demonstrates how the atomic movement correlates with their original position. For NP with diameter larger than 2 nm, the XACF remains at the value of 1 until it reaches the melting temperature, indicating the atomic vibration around their original location. Meanwhile, the decrease in XACF for 2 nm NP at low temperature indicates the movement away from their origin location, with a significantly smaller magnitude compared to the melting state at 1300 K. Consequently, the formation of facet state occurs due to localized rearrangement.

### 3.2.3. The Size Dependence of Sintering Time

As shown in Figure 9, the sintering time depends on the process of sintering, and the duration of sintering increases with the diameter of NP. This increase shows a similar trend to the stabilized time of the RDF curve. When the diameter of the nanoparticle increases from 2 nm to 6 nm, both the sintering time and the time for RDF curve stabilization increase sharply. This indicates that localized atomic rearrangement driven by relative energy costs a significant amount of time. However, this kind of rearrangement weakens when NP reaches a diameter above 6 nm, and the rate of increase in time cost for these two phenomena slows down. Additionally, when the NP size reaches 15 and 18 nm, the sintering time and stabilized time of the RDF curve remain nearly constant despite an increase in NP diameter. Furthermore, during the Cu-Pd dissimilar nanoparticles ultra-fast sintering process described in this paper, the sintering process is mainly affected by NPs with low melting points.

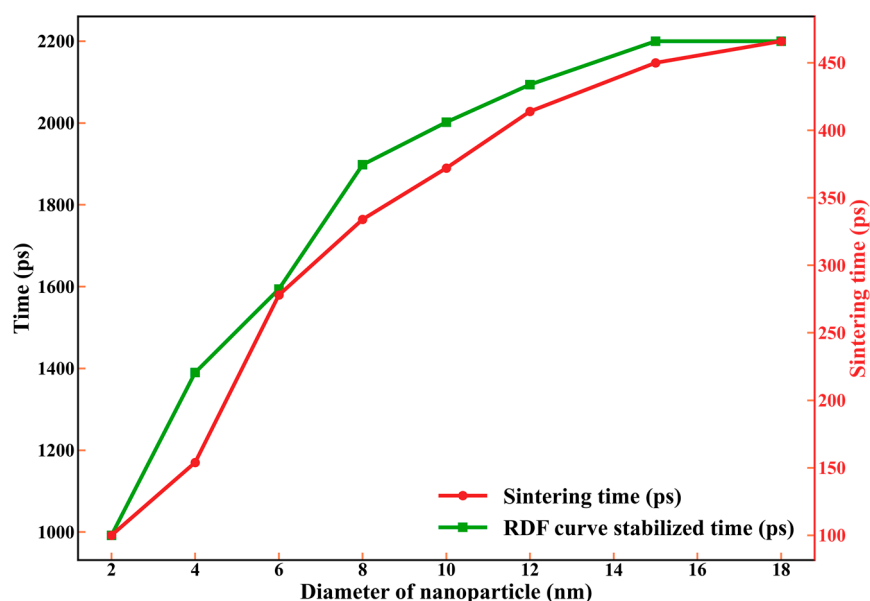


**Figure 9.** The size dependence of the sintering time.

Combining all the results above, we can conclude that the sintering mechanism of two different NPs is size-dependent. For the small NP, the sintering process involves two different mechanisms depending on the sintering temperature. The low-temperature sintering mechanism is related to localized atomic rearrangement driven by relative energy to form the lower-energy facet state rather than the sphere state. Meanwhile, the high-temperature sintering mechanism is governed by surface melting atomic flow. For larger NPs, the sintering process is the same as for small particles at high temperatures due to surface melting atomic flow. Additionally, the sintering process is mainly controlled

by NP with low melting points. After the low melting point metal melts, it will wrap around the high melting one, accelerating the atomic diffusion of the higher melting point at the interface. This atomic dynamic behavior from MD simulation may provide some atomic insight and guide to the specific behavior during the fast heating process of the NP additive coat and high-temperature lubricant, such as Cu and Pd NPs in lubricant additive [78], corrosion-resistant metal film [79], etc.

#### 4. Conclusions

In summary, MD simulations were employed to investigate the atomic movement of Cu-Pd bimetallic nanoparticles based on the MEAM potential with MD tool of LAMMPS and OVITO. During the ultra-fast heating process of heterogeneous Cu-Pd bimetallic nanoparticles, the atomic average potential energy curve, radius of gyration, shrinkage ratio, MSD, NGP, XACF, CNA structure, and other snapshots of the Cu-Pd bimetallic nanoparticles system with diameters ranging from 2–18 nm were studied, and the main conclusions are as follows:

(1) The ultra-fast heating process of Cu-Pd bimetallic nanoparticles has an apparent size effect. For the 2 nm and 4 nm diameter systems, the number of particles is small, the shape is close to the space polyhedron, and the atomic rearrangement phenomenon is clear. The sintering process of the system with a diameter larger than 4 nm presents an apparent “double peak phenomenon”.

(2) The sintering process involves two different mechanisms depending on the sintering temperature. For small particles, the low-temperature sintering mechanism is related to the localized atomic rearrangement driven by the relative energy to form the lower-energy facet state rather than the sphere state. In addition, the high-temperature sintering mechanism is governed by surface melting atomic flow. Moreover, the sintering process is the same as for small particles at high temperatures due to the surface melting atomic flow for large NPs. The sintering process is mainly controlled by NPs with low melting points.

(3) The sintering behavior of the bimetallic nanoparticles under ultra-fast heating rate mainly depend on the low melting NPs. For the nanoparticles larger than 2 nm, the melting of Cu NP is earlier than the Pd NP under the same conditions, and the movement of the shell part of NP is earlier than the core part of NP. The shell part first reaches the melting point, and then drives the core part to reach the melting point.

In addition, the ultra-fast laser sintering process of heterogeneous Cu and Pd bimetallic NPs under different heating rates is noteworthy and needs to be explored in future studies.

**Author Contributions:** Conceptualization, data curation, investigation, validation, visualization, formal analysis, writing—review and editing, Z.Z.; data curation, investigation, writing—review and editing, X.G.; data curation, investigation, writing—review and editing, G.L.; writing—review and editing, H.J.; conceptualization, data curation, investigation, validation, visualization, formal analysis, writing—review and editing, X.F.; conceptualization, investigation, writing—review and editing, S.D. All authors have read and agreed to the published version of the manuscript.

**Funding:** This work was supported by the Innovation Project of Guangxi Graduate Education (YCSW2022063).

**Institutional Review Board Statement:** Not applicable.

**Informed Consent Statement:** Not applicable.

**Data Availability Statement:** The data that support the findings of this study are available from the corresponding authors on reasonable request.

**Acknowledgments:** All calculations were performed in the high-performance computing platform of Guangxi University.

**Conflicts of Interest:** The authors declare no conflict of interest.



## References

1. Tobias, K.; Laurent, M.; Heinz, S.; Walter, R.; Nicholas, D.S.; Heiko, W. Nanoparticle printing with single-particle resolution. *Nat. Nanotechnol.* **2007**, *2*, 9.
2. Jingyu, W.; Tao, X.; Jiahui, G.; Xing, Z.; Yong, Y. A nanogenerator based on metal nanoparticles and magnetic ionic gradients. *NPG Asia Mater.* **2023**, *15*, 1.
3. Lichen, L.; Avelino, C. Metal Catalysts for Heterogeneous Catalysis: From Single Atoms to Nanoclusters and Nanoparticles. *Chem. Rev.* **2018**, *118*, 10.
4. Debroy, T.; Mukherjee, T.; Wei, H.; Elmer, J.W.; Milewski, J.O. Metallurgy, mechanistic models and machine learning in metal printing. *Nat. Rev. Mater.* **2020**, *6*, 1. [[CrossRef](#)]
5. Baptiste, G.; Ann, C.; Oana, C.M.; Patrick, S.; Renelle, D.; Christoph, F.; Surendra, K.M.; Tong, L.; Michael, M.; Julie, M.C. Atom probe tomography. *Rev. Sci. Instrum.* **2007**, *78*, 31101.
6. Parul, C.; Lukman, A.; Anuj, C.; Govind, K.; Wen-Juan, C.; Shaohua, C. Nanoparticle-mediated bioremediation as a powerful weapon in the removal of environmental pollutants. *J. Environ. Chem. Eng.* **2023**, *11*, 109591.
7. Jonas, G.C.; Kimberly, S.B.; Jeffrey, I.Z.; Brinker, C.J. Synthetic amorphous silica nanoparticles: Toxicity, biomedical and environmental implications. *Nat. Rev. Mater.* **2020**, *5*, 886–909.
8. Wei, D.; Bassem, K.; Hong, G.; Hong, L. Roles of nanoparticles in oil lubrication. *Tribol. Int.* **2016**, *102*, 88–98.
9. Tarasov, S.; Kolubaev, A.; Belyaev, S.; Lerner, M.; Tepper, F. Study of friction reduction by nanocopper additives to motor oil. *Wear* **2002**, *252*, 63–69. [[CrossRef](#)]
10. Wu, Y.Y.; Tsui, W.C.; Liu, T.C. Experimental analysis of tribological properties of lubricating oils with nanoparticle additives. *Wear* **2007**, *262*, 819–825. [[CrossRef](#)]
11. Choi, Y.; Lee, C.; Hwang, Y.; Park, M.; Lee, J.; Choi, C.; Jung, M. Tribological behavior of copper nanoparticles as additives in oil. *Curr. Appl. Phys.* **2009**, *9*, e124–e127. [[CrossRef](#)]
12. Chengzhi, H.; Minli, B.; Jizu, L.; Hao, L.; Xiaojie, L. Molecular dynamics investigation of the effect of copper nanoparticle on the solid contact between friction surfaces. *Appl. Surf. Sci.* **2014**, *321*, 302–309.
13. Samuel, B.; Leanne, M.; Jingyi, C.; Robert, A.F.; Min, Z. The effects of polydopamine coated Cu nanoparticles on the tribological properties of polydopamine/PTFE coatings. *Tribol. Int.* **2016**, *103*, 87–94.
14. Guangyuan, L.; Yifei, P.; Zhilei, D.; Ding-Bang, X. Tribology behavior of high-content graphene/nanograined Cu bulk composites from core/shell nanoparticles. *Compos. Commun.* **2021**, *25*, 100777.
15. Tan, H.; Guo, Y.; Wang, D.; Cui, Y. The development of a Cu@Graphite solid lubricant with excellent anti-friction and wear resistant performances in dry condition. *Wear* **2022**, *488*, 204181. [[CrossRef](#)]
16. Sreenivasa, R.P.; Yong, K.W.; Satyanarayana, N.; Sinha, S.K.; Srinivasan, M.P. Tribological properties of nanoparticle-laden ultrathin films formed by covalent molecular assembly. *Langmuir* **2007**, *23*, 8299–8303.
17. Baker, C.C.; Hu, J.J.; Voelodin, A.A. Preparation of Al<sub>2</sub>O<sub>3</sub>/DLC/Au/MoS<sub>2</sub> chameleon coatings for space and ambient environments. *Surf. Coat. Technol.* **2008**, *201*, 4224–4229. [[CrossRef](#)]
18. Reza, S.; Mohsen, A.; Bandar, A.; Roya, K. New nanocomposites containing metal nanoparticles, carbon nanotube and polymer. *J. Nanopart. Res.* **2008**, *10*, 1309–1318.
19. Subramonian, B.; Kato, K.; Adachi, K.; Basu, B. Experimental evaluation of friction and wear properties of solid lubricant coatings on SUS440C steel in liquid nitrogen. *Tribol. Int.* **2005**, *20*, 263–272. [[CrossRef](#)]
20. Hannel, S.; Fouvry, S.; Kapsa, P.; Vincent, L. The fretting sliding transition as a criterion for electrical contact performance. *Wear* **2001**, *249*, 761–770. [[CrossRef](#)]
21. Chanaka, K.; Donovan, N.L.; Harry, M.M.; Huimin, L.; Beth L., A.; Jun, Q. Palladium Nanoparticle-Enabled Ultrathick Tribofilm with Unique Composition. *ACS Appl. Mater. Interfaces* **2018**, *10*, 31804–31812.
22. Jianyong, O.; Yang, Y. Polymer: Metal nanoparticle devices with electrode-sensitive bipolar resistive switchings and their application as nonvolatile memory devices. *Appl. Phys. Lett.* **2010**, *96*, 063506.
23. Wu, Z.P.; Shan, S.Y.; Xie, Z.H.; Kang, N.; Park, K.; Hopkins, E.; Yan, S.; Sharma, A.; Luo, J.; Wang, J. Revealing the Role of Phase Structures of Bimetallic Nanocatalysts in the Oxygen Reduction Reaction. *ACS Catal.* **2018**, *8*, 11302–11313. [[CrossRef](#)]
24. Wang, Y.B.; Tang, W.K.; Wang, F.; Ding, C.P.; Xu, S.M.; Yu, R.H. Effects of surface coating with Cu-Pd on electrochemical properties of A<sub>2</sub>B<sub>7</sub>-type hydrogen storage alloy. *Int. J. Hydrog. Energy* **2018**, *43*, 3244–3252. [[CrossRef](#)]
25. Simchi, A. Effects of lubrication procedure on the consolidation, sintering and microstructural features of powder compacts. *Mater. Des.* **2003**, *24*, 585–594. [[CrossRef](#)]
26. Brahma, N.; Talbot, J. Effects of chemical mechanical planarization slurry additives on the agglomeration of alumina nanoparticles II: Aggregation rate analysis. *J. Colloid Interface Sci.* **2014**, *419*, 25–30. [[CrossRef](#)]
27. Suvankar, G.; Suman, C. Tribological properties of nanoparticle-laden ultrathin films formed by covalent molecular assembly. *Phys. Lett.* **2011**, *375*, 2394–2399.
28. Sajjadnejad, M.; Haghshenas, S.M.S.; Badr, P.; Setoudeh, N.; Hosseinpour, S. Wear and tribological characterization of nickel matrix electrodeposited composites: A review. *Wear* **2021**, *486*, 204098. [[CrossRef](#)]
29. Popov, A.A.; Shubin, Y.V.; Plyusnin, P.E.; Sharafutdinov, M.R.; Korenev, S.V. Experimental redetermination of the Cu-Pd phase diagram. *J. Alloys Compd.* **2019**, *777*, 204–212. [[CrossRef](#)]

30. Yingying, J.; Martial, D.; Shi, J.A.; Hongwei, Y.; Teck, L.T.; Utkur, M. Dynamics of the fcc-to-bcc phase transition in single-crystalline PdCu alloy nanoparticles. *Nat. Commun.* **2023**, *14*, 104.
31. Kateryna, L.; Marc, H.; Matthias, E. Synthesis, Structure, Properties, and Applications of Bimetallic Nanoparticles of Noble Metals. *Adv. Funct. Mater.* **2020**, *30*, 1–14.
32. Panagiotis, G.; Mukhles, S.; Joseph, K. Computational Modeling of Nanoparticle Coalescence. *Adv. Theor. Simul.* **2019**, *2*, 1900013.
33. Junhua, Z.; Guangbin, Y.; Chunli, Z.; Yajuan, Z.; Shengmao, Z.; Pingyu, Z. Synthesis of water-soluble Cu nanoparticles and evaluation of their tribological properties and thermal conductivity as a water-based additive. *Friction* **2019**, *7*, 246–259.
34. Huabing, Y.; Xuecheng, Z.; Zhiwei, G.; Yicong, X.; Xiang, R.; Chengqing, Y. Synergetic effects of surface textures with modified copper nanoparticles lubricant additives on the tribological properties of cylinder liner-piston ring. *Tribol. Int.* **2023**, *178*, 108085.
35. Sánchez-López, J.C.; Abad, M.D.; Kolodziejczyk, L.; Guerrero, E.; Fernández, A. Surface-modified Pd and Au nanoparticles for anti-wear applications. *Tribol. Int.* **2011**, *44*, 720–726. [[CrossRef](#)]
36. Abad, M.D.; Sánchez-López, J.C. Tribological properties of surface-modified Pd nanoparticles for electrical contacts. *Wear* **2013**, *297*, 943–951. [[CrossRef](#)]
37. Kart, H.H.; Yildirim, H.; Kart, S.O.; Çağın, T. Physical properties of Cu nanoparticles: A molecular dynamics study. *Mater. Chem. Phys.* **2014**, *147*, 204–212. [[CrossRef](#)]
38. Motlagh, M.B.; Kalteh, M. Molecular dynamics simulation of nanofluid convective heat transfer in a nanochannel: Effect of nanoparticles shape, aggregation and wall roughness. *J. Mol. Liq.* **2020**, *318*, 114028. [[CrossRef](#)]
39. Maryam, A.; Movaffaq, K.; Pirooz, M. Determining phase transition using potential energy distribution and surface energy of Pd nanoparticles. *Comp. Mater. Sci.* **2019**, *171*, 109214.
40. Felipe, J.V.; Benjamín, P.; Miguel, K.; Carlos, J.R.; Eduardo, M.B.; José, R. Nanoindentation of polycrystalline Pd hollow nanoparticles: Grain size role. *Comp. Mater. Sci.* **2020**, *179*, 109642.
41. Kang, H.Y.; Wang, H.P. Growth of CuPd nanoalloys encapsulated in carbon-shell. *J. Nanopart. Res.* **2013**, *15*, 1672. [[CrossRef](#)]
42. Caroline, D.; Jerome, D. Effect of the Composition on the Free Energy of Crystal Nucleation for CuPd Nanoalloys. *J. Phys. Chem. A* **2016**, *120*, 27657–27664.
43. Fatih, A.C.; Ebru, T.K. Molecular dynamic investigation of the effect of atomic polyhedrons on crystallization mechanism for Cu-based Cu-Pd and Cu-Pt alloys. *J. Mol. Liq.* **2020**, *314*, 113636.
44. Aidan, P.T.; Aktulga, H.M.; Richard, B.; Dan, S.B.; Brown, W.M.; Paul, S.C.; Pieter, J.V.; Axel, K.; Stan, G.M.; Trung, D.N.; et al. LAMMPS—A flexible simulation tool for particle-based materials modeling at the atomic, meso, and continuum scales. *Comput. Phys. Commun.* **2022**, *271*, 108171.
45. Ga-Un, J.; Chang, S.P.; Hyeon-Seok, D.; Seul-Mi, P.; Byeong-Joo, L. Second nearest-neighbor modified embedded-atom method interatomic potentials for the Pd-M (M = Al, Co, Cu, Fe, Mo, Ni, Ti) binary systems. *CALPHAD* **2018**, *62*, 172–186.
46. Panagiotis, G.; Cathal, C.; Vidyadhar, S.; Mukhles, S. Coalescence-induced crystallisation wave in Pd nanoparticles. *Sci. Rep.* **2014**, *4*, 5779.
47. Denis, J.E.; Brad, L.H. The Nose-Hoover thermostat. *J. Phys. Chem. A* **1985**, *83*, 4069–4074.
48. Berendsen, H.J.; Postma, J.V.; Van Gunsteren, W.F.; DiNola, A.R.H.J.; Haak, J.R. Molecular dynamics with coupling to an external bath. *J. Chem. Phys.* **1984**, *81*, 3684. [[CrossRef](#)]
49. William, C.S.; Hans, C.A.; Peter, H.B.; Kent, R.W. A computer simulation method for the calculation of equilibrium constants for the formation of physical clusters of molecules: Application to small water clusters. *J. Chem. Phys.* **1982**, *76*, 637–649.
50. Andrew, R.L. *Molecular Modelling: Principles and Applications*, 2nd ed.; Pearson Education-Hall: London, UK, 2001.
51. Helio, T.; Paulo, S.B.; José, P.R. Structural characterization of deformed crystals by analysis of common atomic neighborhood. *Comp. Mater. Sci.* **2007**, *177*, 518–523.
52. Stukowski, A. Visualization and analysis of atomistic simulation data with OVITO—the Open Visualization Tool. *Model. Simul. Mater. Sci.* **2010**, *18*, 015012. [[CrossRef](#)]
53. Huilong, Z.; Averbach, R.S. Sintering processes of two nanoparticles: A study by molecular dynamics simulations. *Philos. Mag. Lett.* **1996**, *73*, 27–33.
54. Jun, J.; Pengwan, C.; Jiali, Q.; Weifu, S.; Sergei, A.C.; Alexander, A.M.; Galina, B.M.; Tatiana, A.K. The effect of heating rate on the sintering of aluminum nanospheres. *Phys. Chem. Chem. Phys.* **2021**, *23*, 11684–11697.
55. Qiang, J.; Guisheng, Z.; Hongqiang, Z.; Wengan, W.; Hui, R.; Zhanwen, A.; Zhongyang, D.; Shaohua, Y.; Daozhi, S.; Lei, L. Sintering mechanism of Ag-Pd nanoalloy film for power electronic packaging. *Appl. Surf. Sci.* **2021**, *554*, 149579.
56. Hamed, A.; Hamzeh, Y.; Amir, N.S.; Farid, T. Effects of gas adsorption on the graphite-supported Ag nanoclusters: A molecular dynamics study. *J. Phys. Chem. C* **2013**, *117*, 26287–26294.
57. Song, P.; Wen, D. Molecular dynamics simulation of the sintering of metallic nanoparticles. *J. Nanoparticle Res.* **2010**, *12*, 823–829. [[CrossRef](#)]
58. Jun, J.; Pengwan, C.; Jiali, Q.; Weifu, S.; Sergei, A.C.; Alexander, A.M.; Galina, B.M.; Tatiana, A.K. Dynamic mechanical contact behaviors and sintering mechanism of Al nanoparticles subjected to high-speed impact. *Mater. Chem. Phys.* **2021**, *273*, 125111.
59. Bai, X.M.; Li, M. Ring-diffusion mediated homogeneous melting in the superheating regime. *Phys. Rev. B* **2008**, *77*, 134109. [[CrossRef](#)]
60. Surajit, S.; Soumya, C. Classical relaxation in a double well. *Phys. A* **1994**, *209*, 410–421.

61. Walter, K.; Claudio, D.; Steven, J.P.; Peter, H.P.; Sharon, C.G. Dynamical heterogeneities in a supercooled Lennard-Jones liquid. *Phys. Rev. Lett.* **1997**, *79*, 2827–2830.
62. Rahman, A. Correlations in the motion of atoms in liquid argon. *Phys. Rev.* **1964**, *136*, A405–A411. [[CrossRef](#)]
63. Xue, F.; Deng, P.; Mo, L. Rethinking Lindemann criterion: A molecular dynamics simulation of surface mediated melting. *Acta Mater.* **2020**, *193*, 280–290.
64. Watanabe, M.; Adachi, M.; Fukuyama, H. Correlation between excess volume and thermodynamic functions of liquid Pd-X (X = Fe, Cu and Ni) binary systems. *J. Chem. Thermodyn.* **2019**, *130*, 9–16. [[CrossRef](#)]
65. Liang, T.S.; Zhou, D.J.; Wu, Z.H.; Shi, P.P. Size-dependent melting modes and behaviors of Ag nanoparticles: A molecular dynamics study. *Nanotechnology* **2017**, *28*, 485704. [[CrossRef](#)]
66. Wu, R.; Zhao, X.; Liu, Y. Atomic insights of Cu nanoparticles melting and sintering behavior in Cu-Cu direct bonding. *Mater. Des.* **2021**, *197*, 109240. [[CrossRef](#)]
67. Musazadeh, M.H.; Dehghani, K. The Effect of Crystallographic Orientation on Sintering Behavior of Ni Nanoparticles: A Molecular Dynamic Study. *J. Comput. Theor. Nanosci.* **2013**, *10*, 1497–1502. [[CrossRef](#)]
68. Lange, A.P.; Samanta, A.; Majidi, H.; Mahajan, S.; Ging, J.; Olson, T.Y.; Benthem, V.K.; Elhadj, S. Dislocation mediated alignment during metal nanoparticle coalescence. *Acta Mater.* **2016**, *120*, 364–378. [[CrossRef](#)]
69. Tavakol, M.; Mahnama, M.; Naghdabadi, R. Mechanisms Governing Microstructural Evolution during Consolidation of Nanoparticles. *Mater. Manuf. Process.* **2015**, *30*, 1397–1402. [[CrossRef](#)]
70. Jun, J.; Pengwan, C.; Weifu, S. Monitoring micro-structural evolution during aluminum sintering and understanding the sintering mechanism of aluminum nanoparticles: A molecular dynamics study. *J. Mater. Sci. Technol.* **2020**, *57*, 92–100.
71. Abedini, A.; Montazeri, A.; Malti, A.; Kardani, A. Mechanical properties are affected by coalescence mechanisms during sintering of metal powders: Case study of Al-Cu nanoparticles by molecular dynamics simulation. *Powder Technol.* **2022**, *405*, 117567. [[CrossRef](#)]
72. Eleskandarany, M.S. *Mechanical Alloying: Nanotechnology, Materials Science and Powder Metallurgy*, 2nd ed.; Elsevier: Waltham, MA, USA, 2015.
73. Yi, Z.; Jing, Z. Sintering phenomena and mechanical strength of nickel based materials in direct metal laser sintering process: A molecular dynamics study. *J. Mater. Res.* **2016**, *31*, 2233–2243.
74. Yang, Y.; Zhang, H.; Douglas, J.F. Origin and nature of spontaneous shape fluctuations in “small” nanoparticles. *ACS Nano* **2014**, *8*, 7465–7477. [[CrossRef](#)] [[PubMed](#)]
75. Xue, F.; Deng, P.; Mo, L. Melting of bcc crystal Ta without the Lindemann criterion. *J. Phys-Condens. Matter* **2019**, *31*, 095402.
76. Gao, M.C.; Ouyang, L.Z.; Dogan, O.N. First principles screening of B2 stabilizers in CuPd-based hydrogen separation membranes: (1) Substitution for Pd. *J. Alloys Compd.* **2013**, *574*, 368–376. [[CrossRef](#)]
77. Ercolessi, F.; Andreoni, W.; Tosatti, E. Melting of small gold particles: Mechanism and size effects. *Phys. Rev. Lett.* **1991**, *66*, 911–914. [[CrossRef](#)]
78. Pernilla, T.; Paul, E. Hydrogen-Driven Surface Segregation in Pd Alloys from Atomic Scale Simulations. *J. Phys. Chem. C* **2021**, *125*, 17248–17260.
79. Gao, X.; Tang, J.L.; Zuo, Y.; Tang, Y.M.; Xiong, J.P. The electroplated palladium–copper alloy film on 316L stainless steel and its corrosion resistance in mixture of acetic and formic acids. *Corros. Sci.* **2009**, *51*, 1822–1827. [[CrossRef](#)]

**Disclaimer/Publisher’s Note:** The statements, opinions and data contained in all publications are solely those of the individual author(s) and contributor(s) and not of MDPI and/or the editor(s). MDPI and/or the editor(s) disclaim responsibility for any injury to people or property resulting from any ideas, methods, instructions or products referred to in the content.